Plasma surface engineering of graphite and its effect on advancing the performance of aluminium battery

Carbon 245 (2025) 120835

Contents lists available at ScienceDirect

Carbon

journal homepage: www.elsevier.com/locate/carbon

Plasma surface engineering of graphite and its effect on advancing the performance of aluminium battery

Ruiqi Chen [a,1], Neelakandan M. Santhosh [b,c,1], Janez Zavašnik [b,d], Ravi Kumar Trivedi [e,f], Saju Joseph [g], Komal Gola [a], Nitish Kumar [a], Uroš Cvelbar [b,c,*], Jinhua Sun [a,**]

[a] Department of Industrial and Materials Science, Chalmers University of Technology, SE-412 96, Göteborg, Sweden
[b] Department of Gaseous Electronics (F6), Jožef Stefan Institute, Jamova 39, Ljubljana, SI-1000, Slovenia
[c] Jožef Stefan International Postgraduate School, Jamova 39, Ljubljana, SI-1000, Slovenia
[d] Max-Planck-Institut für Nachhaltige Materialien, Max-Planck-Straße 1, 40237, Düsseldorf, Germany
[e] Department of Physics, Karpagam Academy of Higher Education, Coimbatore, 641021, Tamil Nadu, India
[f] Centre for Computational Physics, Department of Physics, Karpagam Academy of Higher Education, Coimbatore, 641021, Tamil Nadu, India
[g] School of Nanoscience and Nanotechnology, Mahatma Gandhi University, Kottayam, 686560, Kerala, India

ARTICLE INFO

Keywords:
Plasma surface engineering
Aluminium batteries
Graphite
Intercalation
Storage mechanism

ABSTRACT

Aluminium batteries, with high gravimetric capacities and cost-effective aluminium metal anodes, are a promising alternative to the existing energy storage devices. Graphite is a frontrunner among variously explored cathode active materials due to its high electrical conductivity and ability to accommodate chloroaluminate anions for non-aqueous aluminium batteries. However, the quality of graphite, surface chemistry, contamination, and various structures affect the performance differently. Particularly, the graphite surface significantly influences the fast intercalation of aluminium anions. Here, we put forward a fast and facile plasma-enabled surface engineering strategy to tailor the commercial graphite flakes to investigate their effect on the storage capabilities of chloroaluminate anions. A mild hydrogen and argon plasma was used to engineer the graphite surface and tailor the structural quality. Notably, the hydrogen plasma-treated graphite exhibits a significant increase in electrochemical performance by delivering a remarkable specific capacity (132.68 mAh/g at 50 mA/g) and excellent high-rate performance (83.94 mAh/g at 1000 mA/g) with good stability. Ex-situ Raman and X-ray photoelectron spectroscopy studies showed that plasma surface tailoring allows the fast intercalation of the chloroaluminate. The controlled plasma surface treatment on graphite directs the fundamental understanding of the basic principles of intercalation chemistry of chloroaluminate in graphite via the surface. The effect of the surface treatment on the ion intercalation and energy storage capability was confirmed and demonstrated by the density functional theory calculation. Such a finding would pave a new path to developing practical aluminium batteries using commercially available graphite.

1. Introduction

Developing high-performance energy storage technologies is highly desirable due to the ever-increasing demand for sustainable and clean energy. Lithium-ion batteries (LIBs) are the most popular and dominant rechargeable batteries, considering their advantages, such as high energy density, long cycle life, and low self-discharge rates, which make LIBs competitive over most other commercialised energy storage technologies [1]. However, they also face challenges and limitations, such as high costs, safety issues, the need for critical metal elements, and environmental impacts [2,3]. The development of alternative energy storage technology is an important research focus in the energy storage field. Multivalent ion batteries (MIBs) with better cycling stability, lower cost, improved safety, and, more importantly, abundant elements have attracted significant attention as an alternative new energy storage technology to complement the limitations of LIBs [4,5]. Among various

* Corresponding author. Department of Gaseous Electronics (F6), Jožef Stefan Institute, Jamova 39, Ljubljana, SI-1000, Slovenia. Jožef Stefan International Postgraduate School, Jamova 39, Ljubljana, SI-1000, Slovenia.
** Corresponding author. Department of Industrial and Materials Science, Chalmers University of Technology, SE-412 96, Göteborg, Sweden.
E-mail addresses: uros.cvelbar@ijs.si (U. Cvelbar), jinhua@chalmers.se (J. Sun).
[1] Equal Contribution.

https://doi.org/10.1016/j.carbon.2025.120835
Received 22 July 2025; Received in revised form 11 September 2025; Accepted 11 September 2025
Available online 12 September 2025

MIBs, aluminium batteries stand out due to their competitive advantages, such as the remarkable volume and mass-specific capacity of aluminium (8040 mA h/cm^3 and 2980 mA h/g), fast charging capability and the abundance of aluminium for electrode materials [6]. In addition, aluminium metal is also non-flammable, nontoxic, low cost, and stable in the air, making it cost-effective and sustainable in battery cell manufacturing, in contrast with the high cost and energy consumption of LIB cell manufacturing [7]. Considering that the energy density of a battery is determined by the combined effect of anode and cathode, a proper evaluation of cathode materials for each anode needs to be undertaken to understand the impact of aluminium-based charge carriers on energy density. However, the lack of high-performance and reliable cathode materials is still the bottleneck that hinders the practical application of aluminium batteries.

Design strategies for cathode materials for aluminium batteries depend on the intercalation chemistry. Material that allows intercalation/deintercalation of numerous compounds at high potentials is desired to design potential cathode materials. Layered material with higher conductivity, surface area, and controllable interlayer distance is preferable for the intercalation of the aluminium-based charge carriers. Among the various layered structures, graphite has been well studied as a cathode active material for aluminium batteries due to its high electrical conductivity, stability during charge-discharge cycles, and low cost [8,9]. The layered structure of graphite enables effective intercalation of chloroaluminate anions ($AlCl_4^-$ and $Al_2Cl_7^-$). However, in the literature, the reported specific capacity of graphite for aluminium batteries varies from 70 mAh/g at 20 mA/g to 115 mAh/g at 60 mA/g in different reports [8,10]. Numerous approaches have been conducted to understand the relationship between the structure of different graphite (e.g., natural graphite, synthetic graphite, and pyrolytic graphite) and their electrochemical properties. It has been demonstrated that natural graphite exhibits the highest specific capacity at all potentials with better capacity retention [10]. The unique structure with highly oriented graphene has been demonstrated as a favourable cathode material for high-performance aluminium batteries with a capacity of 120 mAh/g after a quarter-million cycle at 100 A/g [11].

The research related to the aluminium battery focuses on investigating the bulk electrochemical performance of the different graphitic materials with a combination of various electrolytes and additives [11]. Regarding improving the performance, the previous research efforts were mainly dedicated to modifying the structure of different types of graphite, e.g., expanded graphite, fluorinated natural graphite, and graphene [12], along with understanding their energy storage mechanism [13]. Apart from these features, the surface chemistry of graphite also plays an important role in the performance of aluminium batteries since the $AlCl_4^-$ starts to intercalate from the surface of the graphite. However, the impact of the graphite surface on the performance (e.g., stability, fast charging capability and specific capacity) and the corresponding rational tailor of the graphite surface was rarely studied, although it has been theoretically predicted that open graphite edges and flaky morphology with preserved pristine crystalline structures were crucial for achieving such high charge-storage capacity [9,14]. Notably, this could be one of the most cost-effective strategies to improve the performance of general natural graphite from different sources, making it favourable for direct use in the practical application for aluminium battery.

Owing to the formation of numerous active sites on graphitic materials after the surface modification, the intercalation of ions/electrons into the active material is enhanced with a relatively shorter diffusion path during the charging/discharging process. Subsequently, the specific capacity could be increased while maintaining a favourable charge voltage plateau without parasitic reactions. Compared to different surface modification techniques, plasma-enabled surface engineering allows one of the fastest controllable processes. Plasma is an ionised gas discharge generated by applying a strong electromagnetic field and forms numerous species, such as electrons, ions, photons, and radicals [15]. Interaction of any nanomaterial with these plasma species induces structural defects or targeted functionalisation that could act as an active site for energy storage. Among the different reactive precursors used to generate plasma, hydrogen is considered to modify the surface of carbon nanomaterials by selectively etching the surface [16]. The H atoms have a higher affinity to react with amorphous carbon (a-C) atoms than the sp^2 hybridised carbon atoms and promote the removal of the a-C phase to produce highly crystalline carbon structures [17]. Similarly, the plasma treatment can induce structural defects (vacancy defects or foreign atoms) in the carbon materials and enhance the electrical properties [18]. Therefore, optimising suitable plasma conditions to fine-tune the surface of graphite and manipulating the surface functionalities would be greatly beneficial for advancing energy storage in AIBs.

In this study, we propose a plasma-enabled fast and facile surface engineering strategy for the controlled surface modification of commercially available graphite flakes to improve the performance of aluminium batteries. A mild hydrogen and argon plasma was used as the medium for engineering the graphite surface and controllably tailoring the surface properties. By tailoring the surface characteristics of graphite with hydrogen plasma, the most favourable graphite configuration was optimised and tested for aluminium battery. The hydrogen plasma-treated graphite structures show higher capacity by delivering 132.68 mAh/g at a current density of 50 mA/g and demonstrate excellent stability over cycling for 1000 cycles by maintaining 98 % of initial capacity at a high current density of 500 mA/g. The proposed plasma surface engineering mechanism is one of the fastest techniques to tailor the graphite surfaces and delivers comparable capacity and stability to other state-of-the-art graphite-based electrodes. Such methods could open a new platform for controllably engineering the surface of graphite to enhance the metal ion storage capabilities for future MIBs.

2. Materials and methods

2.1. Preparation of samples

The commercial graphite flakes (325 mesh size, 99.8 %, Alfa Aesar) were used as the starting material. The graphite flakes placed in a ceramic crucible were subjected to plasma surface engineering to improve the charge storage capabilities. Plasma tailoring was conducted in a low-pressure radio-frequency (RF) plasma system, which was an 80 cm-long glass tube with a diameter of 4 cm. The RF generator was inductively coupled through a nine-turn internally water-cooled inductive coil. The graphite flakes in the crucible are placed in the centre of the coil, and the chamber is pumped down to 2 Pa. Later, the reactive gases, argon, hydrogen, nitrogen, and their mixture, were fed into the system at a flow rate of 100 sccm, and the total pressure inside the chamber was maintained between 26 and 32 Pa. In the final stage, the plasma was ignited at 200 W, and the graphite flakes were treated for 6 min. The treatment was conducted incrementally with a period of 2 min three times to prevent the overheating of the material. The samples were labelled as graphite (Gr), H_2 plasma-treated graphite (Gr-H_2), H_2S-plasma-treated graphite (Gr-H_2S; Gas composition was Ar+2 % of H_2S) and Ar-plasma-treated graphite (Ar–H_2). The capacity of Gr-H_2S is very low and the performance is not very reliable, thus this sample was not selected for the further study.

2.2. Physico-chemical characterisation

A scanning electron microscope (SEM; Prisma E, Thermo Fisher Scientific Inc) was used to investigate the surface morphology of the graphite flakes and plasma-engineered graphite flakes. The effect of the plasma treatment on the structural quality of graphite flakes was analysed by Raman spectroscopy (confocal Raman spectrometer; NTEGRA, NT-MDT). The spectra were recorded at an excitation wavelength of 488 nm at multiple points to evaluate the homogeneity. Chemical changes

and functionalities of the samples were identified using X-ray photoelectron spectroscopy (XPS; PHI-TFA XPS spectrometer equipped with Al-monochromatic X-ray source at an energy of 1486.6 ev, Physical Electronics Inc). X-ray Diffraction (XRD, Discovery D8, Bruker) was used to characterise the graphite before and after the plasma treatment.

2.3. Electrodes preparation

The prepared graphite-related materials were separately mixed with the conductive additives of acetylene black and the binder CMC/SBR (mass ratio 1:1) in the planetary mixer at a mass ratio of 80: 10:10. A certain amount of water was then added to form a slurry, which was coated onto the surface of molybdenum foil with a diameter of 12 mm. The coated electrodes were dried in the vacuum oven at 80 °C for 12 h. The areal mass loading of the electrode is 1–1.7 mg/cm^2.

2.4. Electrochemical measurements

The aluminium ion batteries are assembled in an argon-filled glove box. The as-prepared graphite-related electrodes were used as the cathode, aluminium foil was used as the anode, and glass fiber was used as the separator. The ionic liquid electrolyte composed of aluminium chloride ($AlCl_3$) and 1-ethyl-3-methylimidazolium chloride ([EMIm]Cl) with a molar ratio of 1.3:1 was used. The electrochemical measurements were conducted using modified Swagelok-type cells. A molybdenum rod and a glassy carbon rod were used as the current collectors for the anode and cathode, respectively. The galvanostatic measurements, cyclic voltammetry (CV), and electrochemical impedance spectroscopy (EIS) analysis were performed using a Biologic battery cycler. The initial electrochemical performances of all the graphite samples were analysed by the Galvanostatic charge-discharge (GCD) to optimise the best cathode materials and presented in Fig. S1.

2.5. Ex-situ characterisations of electrodes

For ex-situ Raman, XPS, and XRD characterisations, the cells were disassembled in the argon-filled glovebox at different potentials and washed with ethanol to remove the residual absorbed electrolyte. Then the electrodes were dried under vacuum before being used for ex-situ measurements.

2.6. Computational methodology

Vienna Ab-initio simulation package (VASP) [1–4] within the projector augmented wave (PAW), and the exchange correlation functional described by the generalised gradient approximation (GGA) [5] was used to carry out all the geometry relaxations to support the experimental observation. The intercalation behavior of $AlCl_4^-$ anion was examined in both crystalline graphite and amorphous graphite. A hexagonal graphite supercell with a d spacing of around 9.12 Å [6] to accommodate the $AlCl_4^-$ anion, and the d spacing is 4.56 Å between two graphene layers, was considered for the calculations.

3. Results and discussion

3.1. Structural characterisations and chemical composition analysis

Considering the Gr-Ar and Gr-H_2-based cathodes demonstrated better electrochemical performance during the initial GCDs (Fig. S1), the physico-chemical characterisations were conducted on those structures to understand the charge storage mechanism. Different surface analysis techniques have been conducted to understand the changes in the surface and chemical composition of the graphite flakes after the plasma surface treatment. Considering H_2 and Ar plasma, known as the etchants to remove the amorphous structures from the graphite surface, the samples were evaluated by the SEM to understand the changes in the surface morphology induced by the plasma-enabled etching and ion bombardment. The representative micrographs of the surface morphology of the graphite and plasma surface-treated graphite are summarised in Fig. 1a–c. The non-treated graphite structures feature large multi-layered flakes. The plasma-treated graphite structures have a cleaner surface than the controlled samples, which could be due to the plasma-induced etching of the topmost layers. However, no severe damages were observed on the surface, indicating that the mild plasma treatment gently removed the carbonaceous ripples from the graphite surface, which would benefit the chloroaluminate intercalation by reducing the charge transport pathway during the electrochemical reaction. Besides, it is observed that several small graphite flakes are also present after the plasma treatment, which will boost the rate performance and cycling performance owing to their open graphite edges and reduced thickness [19]. After hydrogen plasma treatment, the graphite reduced about 2.8 wt%, verifying the removal of impurities, amorphous carbon and functional groups from the graphite.

The samples were further analysed to identify enhancements in the structural quality of the materials. The structural organisation of the samples was evaluated by Raman spectroscopy, and the results are presented in Fig. 1d. All the samples have graphene-like structure features, and the major peaks were observed at 1358 (D band), 1583 (G band), 1614 (D′ band), and 2718 (2D band) cm^{-1}. Considering that the plasma-treated samples have a cleaner surface, an in-depth analysis of the Raman spectra was conducted by deconvoluting the peak area of the D and G regions. The changes in the defect ratio (I_D/I_G) of graphite after the plasma treatment were evaluated from the area under the curves of deconvoluted D and G peaks. It is known that the highly crystalline graphitic materials show an intensity ratio between 0.1 and 0.3. In this study, the Gr samples exhibit a ratio of 0.31, which was reduced in Gr-H_2 samples to a minimal ratio of 0.24, while Gr-Ar displays the highest number of 0.34. This indicates that the ion bombardment with heavier Ar species increases the surface defects in the graphite, while H_2 plasma improves the structural quality by the selective removal of the amorphous phases. This selective removal of amorphous carbon (a-C) could be due to the interaction of hydrogen species with a-C, which creates volatile compounds and is removed during surface treatment. In addition, the D' (1614 cm^{-1}) band area of the Gr-H_2 was reduced, possibly due to the partial removal of the edge-like structures from the graphite surface.

Therefore, Gr and Gr-H_2 samples were analysed by transmission electron microscope (TEM) (Fig. 2) to understand the major changes on the surface of the graphite flakes, especially the edge surface. The Gr sample shows a large accumulation of carboniferous material (Fig. 2a), identified by SAED as pure graphite. No amorphous phases or other structural modifications were observed. On the edge of the thin sections, multiple stepped surfaces were detected as a result of uneven cleavage, revealing a multi-layered nanostructure (Fig. 2b). These multi-layered features with stepped stair-like edges might contribute to the high intensity of the D′- band in the Raman spectra. On the exposed surfaces, many structural discontinuities, such as ripples and structural defects, can be observed. The very edge of the thin section reveals rippled edges even at the nanoscale (Fig. 2c). In the case of the Gr-H_2 sample, the overview micrographs show several-layer thick graphite crystallites (Fig. 2d). The surface seems pristine, with the remains of the surface ripples observed only sporadically, which could be due to the H_2-plasma-induced removal of the ripples from the surface of Gr. (Fig. 2e). Contrary to the untreated sample, bending of the thin sheets, revealing the characteristic edge periodic structures, is common (Fig. 2f). The comparison of the SAED ring patterns with the simulated reference pattern shows a good match (Fig. 2g). The detailed analysis of the reflection peak positions and comparison with the reference data shows there is no difference in the inter-layer (in c-axis direction, i.e., reflections from the (002) planes) or infra-layer interatomic distances (the (101) and (110) planes), as the reflection peaks match with the pure graphite structural reference data (Fig. 2h).

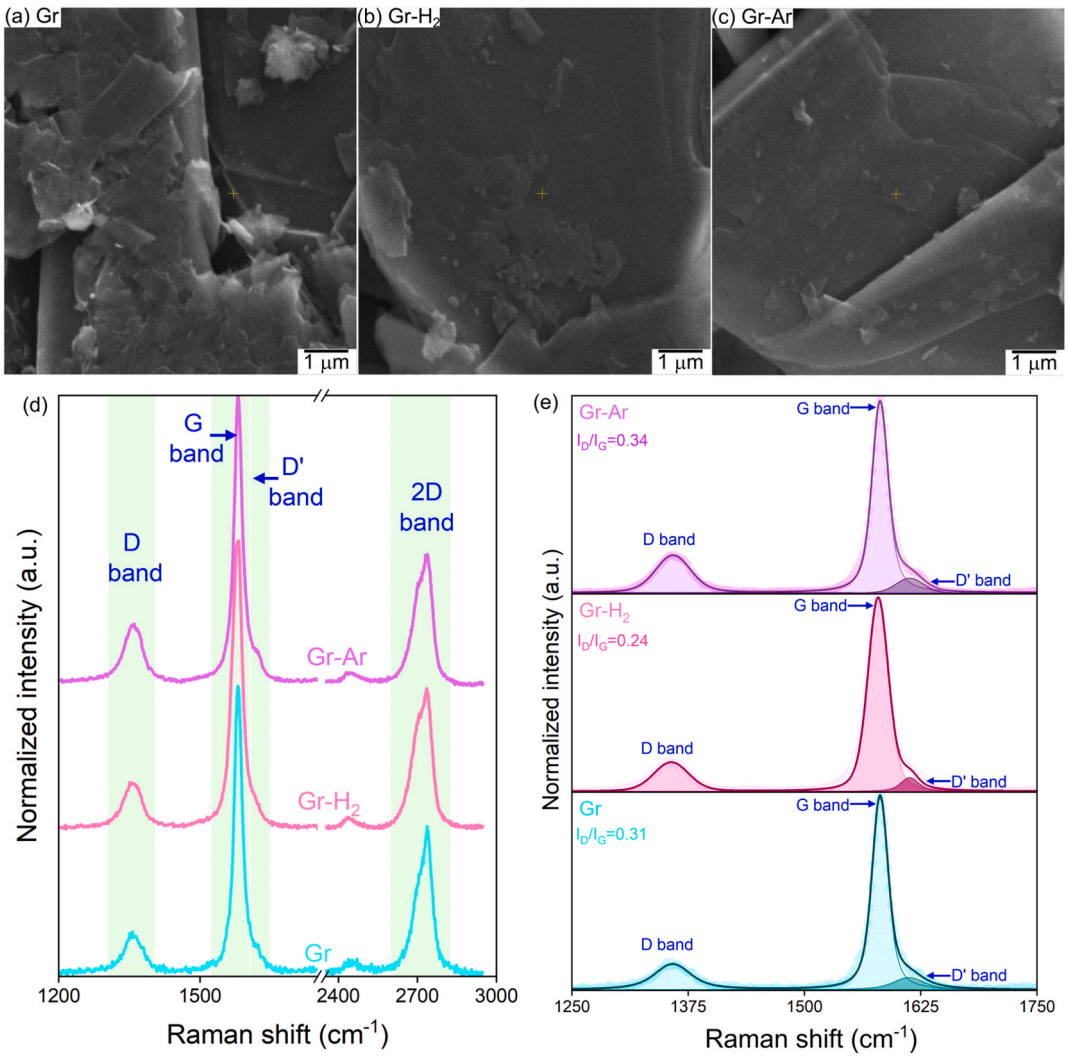

Fig. 1. SEM images of (a) Gr, (b) Gr-H_2, (c) Gr-Ar; (d) Raman spectra and (e) deconvoluted D and G regions of graphite and plasma-tailored graphite.

Furthermore, some black spots are observed as under-focused spots on Gr-H_2 under the electron beam (Fig. 2e), probably due to vacancies in the layer. Also, the smaller number of steps in the carbon lattice may indicate the decreased intensity of the D' band in the Raman spectra. In order to compare the crystalline features of the Gr and Gr-H_2 structures, the SAED patterns were recorded. The Gr materials displayed a single crystalline feature while Gr-H_2 represents polycrystalline features, which might be due to the continuous etching and layer thinning. Considering that the step-like edge in Gr-H_2 was diminished after plasma treatment, the edge of the graphite could be exposed for the fast intercalation of the $AlCl_4$ anions and enhance the charge storage properties.

As it is seen that the surface of the raw graphite material is improved after the plasma treatment, the changes in the chemical composition were evaluated to further understand the changes in chemical functionalities after the plasma treatment. The XPS survey spectra of all the samples are presented in Fig. 3a, and all the samples featured peaks around 284.8 eV and 532 eV, corresponding to the presence of carbon and oxygen, respectively. It is noticed that the atomic content of oxygen was reduced after both plasma treatments (Table S1), indicating that the surface contaminants were removed in both cases, which could allow the enhanced intercalation during electrochemical reactions. Therefore, to investigate the changes in the chemical bonding in the carbon lattice on the surface of graphite, high-resolution C 1s spectra were evaluated. Comparison of the C 1s spectra of Gr, Gr-Ar and Gr-H_2 indicates a slight change in the 283–284 eV region, in which the peak slightly broadened after the plasma treatment. These broadenings from the pristine graphite could be due to the structural imperfections caused by the plasma-induced structural modification. Such observations also agree with the microscopic and Raman spectroscopic findings. The deconvolution of C 1s spectra of all the samples demonstrates the presence of different carbon groups in the lattice, namely: sp^2 C–C (284.6 eV), sp^3 C–C (285.3 eV), structural defects (283.8 eV), C–OH (286.3 eV), C–*O*–C (287.2 eV), C═O (288.4 eV) and π-π* (291.1 eV) shakeup satellites. It is found that the contribution of the functional groups, apart from the sp^2/sp^3 C–C, has reduced after the plasma treatment, predominantly in Gr-H_2, which could contribute to the improved chloroaluminate intercalation.

The crystal structure of both pristine and plasma-treated samples was examined by X-ray diffraction (XRD). All diffraction patterns match the reference pattern of pure graphite. To assess potential variations in interlayer spacing, such as exfoliation or structural degradation, particular attention was given to the characteristic (002) reflection at $2\theta = 26.59°$ (Fig. 3f). No measurable peak shift was observed, indicating that the graphite lattice remained structurally intact during the plasma treatment. The interlayer distance along the c-axis, calculated using Bragg's law ($d = \frac{\lambda}{2 \sin \theta}$), was found to be 3.34 Å.

All the analyses show that the plasma treatment creates a cleaner surface and alters the structural composition, which could facilitate the charge transfer pathways and chloroaluminate intercalation in aluminium battery. The XPS analysis confirmed that both the plasma

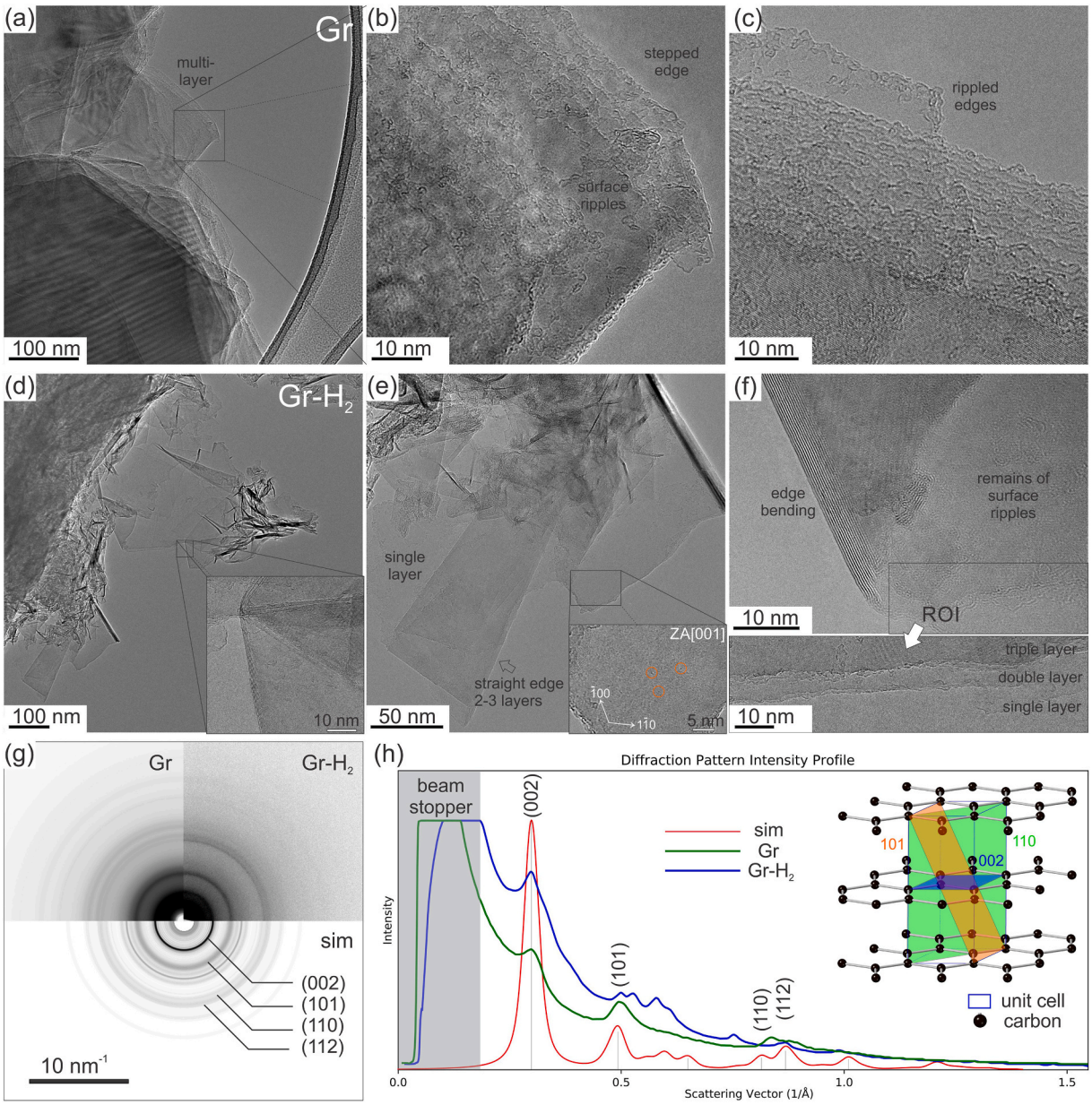

Fig. 2. TEM micrographs of (a–c) Gr and (d–f) Gr-H2, with magnified region and marked main features on the surface and edges. (g) The comparison of experimental and ab-initio simulated Selected Area Electron Diffraction (SAED) ring patterns; main reflection planes are marked on the graphite simulation. (h) Diffraction pattern intensity profile for Gr and Gr-H_2 samples, with simulation profile. The major reflection planes are marked on the structure model.

treatments removed the amorphous carbon and surface oxygen-containing groups. However, compared to the Gr-Ar, the defect density in Gr-H_2 is lower, indicating that the structural distortion was lower in the latter case. Besides, it is identified from the TEM that the step-like edges were cleaned after the H_2 plasma, and the plasma creates some vacancies on the graphene lattice. All these surface changes, including more open edges, surface defects and cleaner graphitic surfaces, could facilitate the intercalation reaction and enhance the charge storage mechanism. Thus, graphite and plasma-treated graphite were tested as efficient cathodes to explore the advantage of plasma in improving the performance of aluminium batteries.

3.2. Electrochemical performance

The use of natural graphite as a cathode material for aluminium batteries has been well studied in terms of the specific capacity, energy storage mechanism, and the correlation between the crystalline structure of graphite and its performance. The effect of surface structure and chemistry on electrochemical performance is systematically investigated below. The electrochemical behaviour of graphite and plasma-treated graphite as cathode materials was evaluated in a standard Swagelok cell using aluminium as anode and an ionic liquid mixed with 1-ethyl-3-methylimidazole hydrochloride and anhydrous aluminium chloride as the electrolyte. The first galvanostatic charge-discharge curves of the original graphite, Gr-Ar, and Gr-H_2 cathode materials at a current density of 100 mA/g are presented in Fig. 4a. The initial charge/discharge specific capacities of graphite, Gr-Ar, and Gr-H_2 are 75.31/67.48, 92.21/79.36, and 129.24/123.85 mA h/g, corresponding to the stoichiometries of $C_{33}(AlCl_4^-)$, $C_{29}(AlCl_4^-)$, and $C_{19}(AlCl_4^-)$, respectively, which is comparable to the reported specific capacity (Table S2) and the calculated stoichiometry [10,20]. The lower columbic efficiency is due to the decomposition of the electrolyte and the trapped ion in the electrode materials, which cause the irreversible reactions [10]. Apparently, the hydrogen-plasma-treated graphite

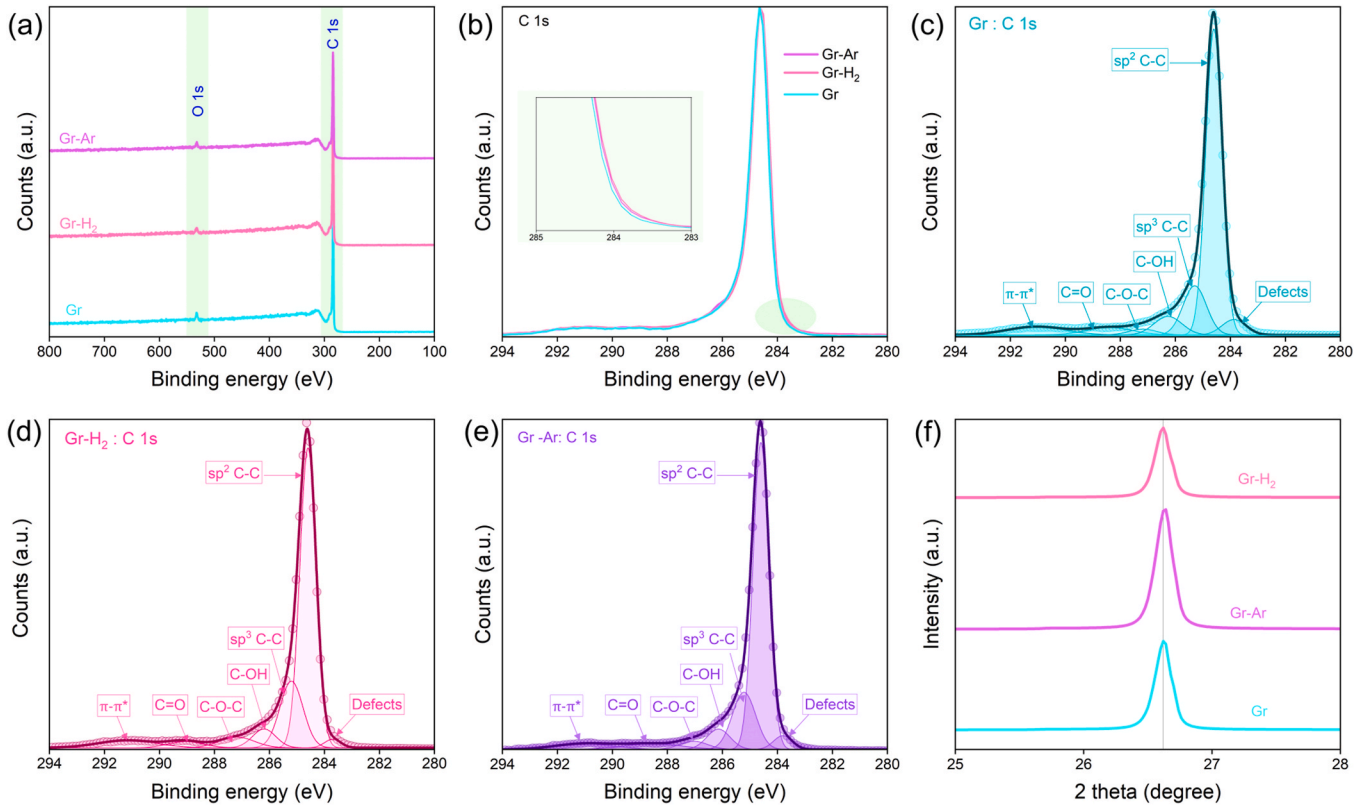

Fig. 3. (a) XPS survey spectra of graphite and plasma tailored graphite flakes; (b) Comparison of high-resolution C 1s spectra with the noticeable changes in the defect region in the inset; deconvoluted C 1s spectra of (c) graphite, (d) H_2-plasma treated graphite and (e) Ar-plasma treated graphite; (f) XRD pattern of pure and plasma engineered graphite around the characteristic (002) diffraction peak.

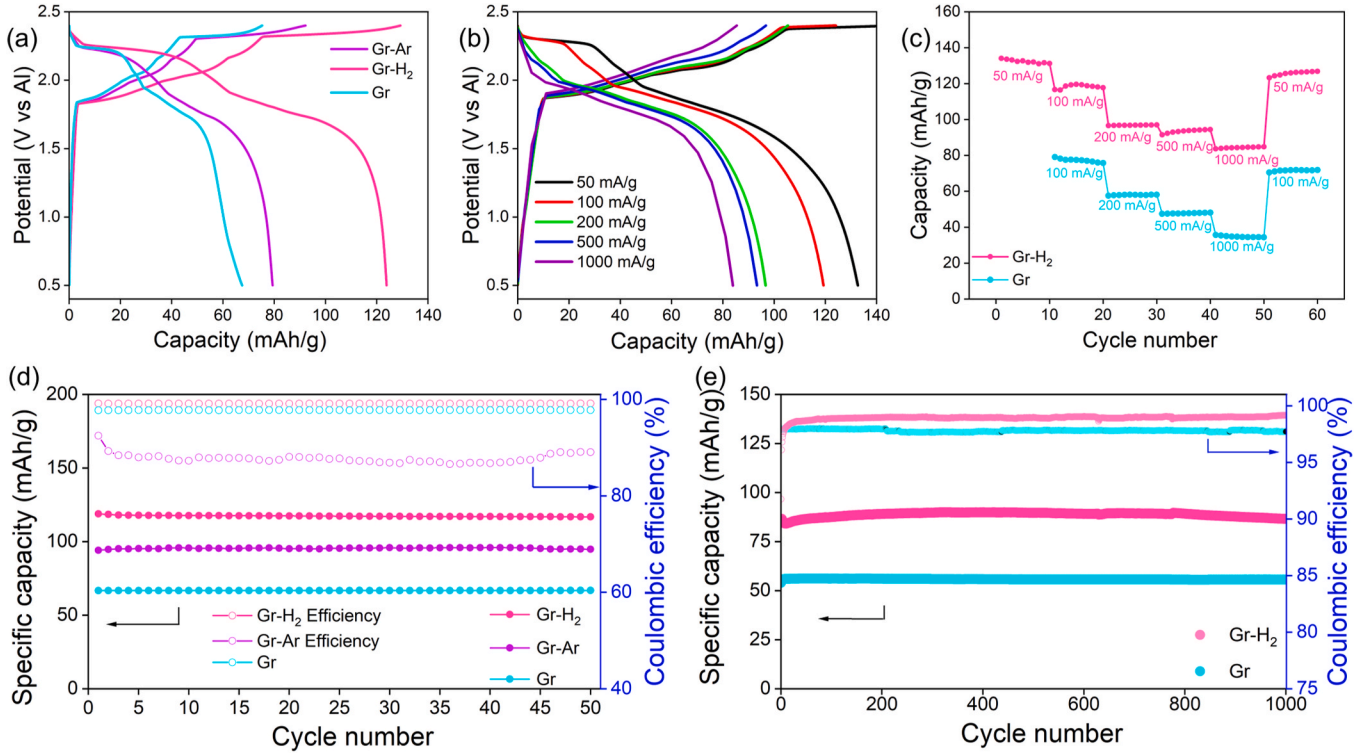

Fig. 4. Electrochemical performance of different plasma treatment graphite samples: (a) The first cycle GCD profiles of Gr-H_2, Gr-Ar, and graphite cathodes; (b) GCD profiles of Gr-H_2 for the first cycle at different current densities; (c) Rate capabilities of Gr-H_2 and graphite cathodes; (d) Cycling performance and Coulombic efficiency of Gr-H_2, Gr-Ar, and Gr cathodes at 100 mA/g for 50 cycles; (e) Cycling performance and Coulombic efficiency of Gr-H_2 and Gr cathodes at 500 mA/g for 1000 cycles.

shows the highest specific capacity. The charge-discharge curves of all three samples exhibit a similar shape, which shows three short voltage platforms at c.a. 1.8, 2.0, and 2.15 V, and the major voltage plateau starts from 2.3 V, which corresponds to the intercalation of $AlCl_4^-$ anions into graphitised structures [21]. The capacity contribution charged from 2.0 to 2.3 V from the Gr-H_2 is two times higher than that of the non-treated graphite and Gr-Ar, which implies that the surface of graphite after hydrogen plasma treatment facilitates the intercalation of the $AlCl_4$ anions, accommodating more $AlCl_4$ anions at high graphite intercalation stages (e.g., stage 4). The chemical functionalities at the surface of original graphite and Gr-Ar may make the intercalation of the $AlCl_4$ anions sluggish, resulting in a lower specific capacity. The hydrogen plasma treatment allows favourable intercalation of the $AlCl_4$ anions from the surface of the Gr-H_2, thus accelerating and promoting the intercalation of $AlCl_4$ anions to reach lower graphite intercalation stages (e.g., stage 1, 2 and 3). The voltage plateau for the discharge curve starts at 2.25 and 1.9 V, which is attributed to the deintercalation of $AlCl_4$ anions. The specific capacity of the Gr-Ar is also higher than that of the original graphite and other types of graphite materials [22]. This might be due to the cleaning effect of the Argon plasma surface treatment, which partially removes the amorphous carbon and contaminations from the surface of the graphite. However, the surface treatment effect of the argon is lower than that of the hydrogen plasma surface treatment because the hydrogen is a strong reducing reagent, while the argon is an inert gas. The hydrogen plasma surface treatment not only removes the surface contaminations but also reduces the amorphous carbon to graphitic carbon (confirmed from the TEM and Raman), resulting in improved electrochemical performance of the $AlCl_4^-$ anions intercalation and storage. Several other factors induced by plasma treatment such as: the much cleaner graphite surface with only sporadically distributed ripples; removal amorphous flakes and presence of small graphitic fakes on the surface; characteristic exposed edge periodic structures in Gr-H_2 visible from the bending of the thin sheets; improved crystalline features with pronounced signals from the edges observed from Raman spectra, are also vital for intercalating $AlCl_4^-$ ions and contributes to enhanced pathways for the charge storage. The columbic efficiency of Gr-H_2 is higher than that of the original graphite and the Gr-Ar. The typical columbic efficiency is also higher than that of most of the reported graphite-related materials for aluminium battery [14,23]. This also provides strong evidence of the cleaning effect of the hydrogen plasma treatment, which reduced the side reactions at the graphite surface during the charging and discharging process.

The first galvanostatic charge-discharge curves of Gr-H_2 cathode materials at various current densities are shown in Fig. 4b. The first charge/discharge specific capacity of Gr-H_2 cathode material at current densities of 50 mA/g, 100 mA/g, 200 mA/g, 500 mA/g, and 1000 mA/g is 147.89/132.68 mA h/g, 124.13/119.28 mA h/g, 105.39/96.72 mA h/g, 96.84/93.30 mA h/g, 85.44/83.94 mA h/g, respectively. A comparison of the electrochemical charge storage of Gr-H_2 cathodes for aluminium batteries with other reported graphite-based electrodes is presented in Table S2 [9,21,24–28]. The comparison between the rate capability of graphite and Gr-H_2 at different current densities is presented in Fig. 4c. The average reversible specific capacity for Gr-H_2 at 50 mA/g is 132.36 mA h/g, and graphite at 100 mA/g is 77.23 mA h/g for 10 cycles. It is worth noting that the graphite cathode cannot be charged to 2.4 V at 50 mA/g (Fig. S2) due to sluggish intercalation, indicating that the side reaction caused by the decomposition of the electrolyte is accelerated at low current density for graphite material [8,25]. With the increase of current density to 1000 mA/g, the average reversible specific capacity decreased to 84.34 mA h/g for the Gr-H_2 cathode and 34.80 mA h/g for the graphite cathode. After 50 cycles at different current densities, the specific capacity of the Gr-H_2 cathode can be recovered to 125.63 mA h/g at 50 mA/g with 95 % retention of capacity. Comparably, the specific capacity of the graphite cathode is restored to 71.51 mA h/g with 92.6 % retention of capacity at 100 mA/g after 40 cycles of rate test. The results demonstrate excellent rate capability and structural stability under cycling for graphite after hydrogen-plasma treatment, which is mainly attributed to the fact that the surface of graphite is modified with plasma, which helps to enhance the affinity between the electrode material and the electrolyte, thereby promoting the fast intercalation/deintercalation of $AlCl_4^-$ anions inside the graphite material.

The cycling stability test results for Gr, Gr-Ar, and Gr-H_2 are represented by Fig. 4d–e and Figure S3-4. For the samples tested at 100 mA/g, as shown in Fig. 4d, the specific capacity remains stable for plasma-treated graphite. After 50 cycles, 98.2 % of the specific capacity is retained from the initial specific capacity of 116.86 mA h/g for the Gr-H_2 cathode, while the specific capacity is only 66.82 mA h/g for the graphite cathode, which may be ascribed to the unstable side reaction. Besides, the coulombic efficiency of Gr-H_2 can be maintained at 99 %. Comparably, the coulombic efficiency of graphite materials is 98 % while Gr-Ar demonstrated a lower coulombic efficiency of 90 %. This lowered efficiency could be due to the side reactions at the surface of the Gr-Ar cathode. Compared with the hydrogen plasma-treated graphite, the original graphite surface has more functional groups, amorphous carbon and impurities, while the Gr-Ar has more defects, which could promote and catalyze the decomposition of the electrolyte, resulting in the formation of the thicker SEI and lower coulombic efficiency. The defect density was higher than the other electrodes, as demonstrated by the Raman spectra. Moreover, such side reactions may induce strong coulombic interaction and hinder the reversible storage and release of the $AlCl_4^-$, further leading to poor coulombic efficiency [29]. The higher coulombic efficiency for Gr-H_2 material demonstrates the relatively stable structure for the intercalation/deintercalation of $AlCl_4^-$ during the charge and discharge cycling processes. The long cycle test at 500 mA/g is illustrated in Fig. 4e. Notably, the Gr-H_2 cathode still maintains a high specific capacity of 86.6 mA h/g after 1000 cycles. As shown in Fig. S3, the GCD curves overlap well from the first cycle to the 1000th cycle, further demonstrating the remarkable stability of the graphitised structure of Gr-H_2 material.

In order to study the electrochemical behaviour and major changes that occur after the plasma treatment, CV curves are measured for Gr and Gr-H_2 materials as the cathode. The CV curves for both materials at 1 mV/s are shown in Fig. 5a, in which the material displays the typical curve shapes of graphite materials from the second cycle (others cycles shown in Fig. S5–8) [30]. It can be observed that the anodic peaks for Gr-H_2 cathode are located at 1.91, 2.13, 2.24, and 2.36 V, corresponding to the intercalation of $AlCl_4^-$ anions in different stages [31]. Meanwhile, four cathodic peaks related to the deintercalation of $AlCl_4^-$ anions appear at 2.21, 2.06, 1.87, and 1.69 V, respectively. When comparing with graphite, the potential peaks separation of Gr-H_2 is lower than that of graphite, indicating plasma-treated graphite possesses better reversibility for the intercalation/deintercalation of $AlCl_4^-$ anions. Besides, the potential positions of anodic and cathodic peaks for the Gr-H_2 cathode are lower, which can demonstrate the hydrogen plasma treatment method, promoting the intercalation/deintercalation behaviour into the graphite cathode.

To understand the electrode/electrolyte interaction, the CV of Gr-H_2 structures tested at different cycles at the scan rate of 0.1 mV/s and is given in Fig. 5b. Fig. S5 shows CVs of graphite for comparison. In the initial cycle, oxidation peaks appear at 2.0, 2.2, and 2.35 V, which are different from the following cycles, indicating the formation of the solide electrolyte interphase (SEI) layer. The peak positions are well aligned with the galvanostatic charge-discharge voltage platform. Besides, the shapes of CV curves are well preserved after 5 cycles, demonstrating the excellent stability of Gr-H_2 cathode materials for aluminium storage.

To further investigate the mechanism of electrochemical storage behavior, CV curves at different scan rates are obtained (Fig. 5c). In the electrochemical study, the energy storage behavior can be explained by two mechanisms: diffusion intercalation control and adsorption capacitance control [32]. The contribution rate of diffusion intercalation

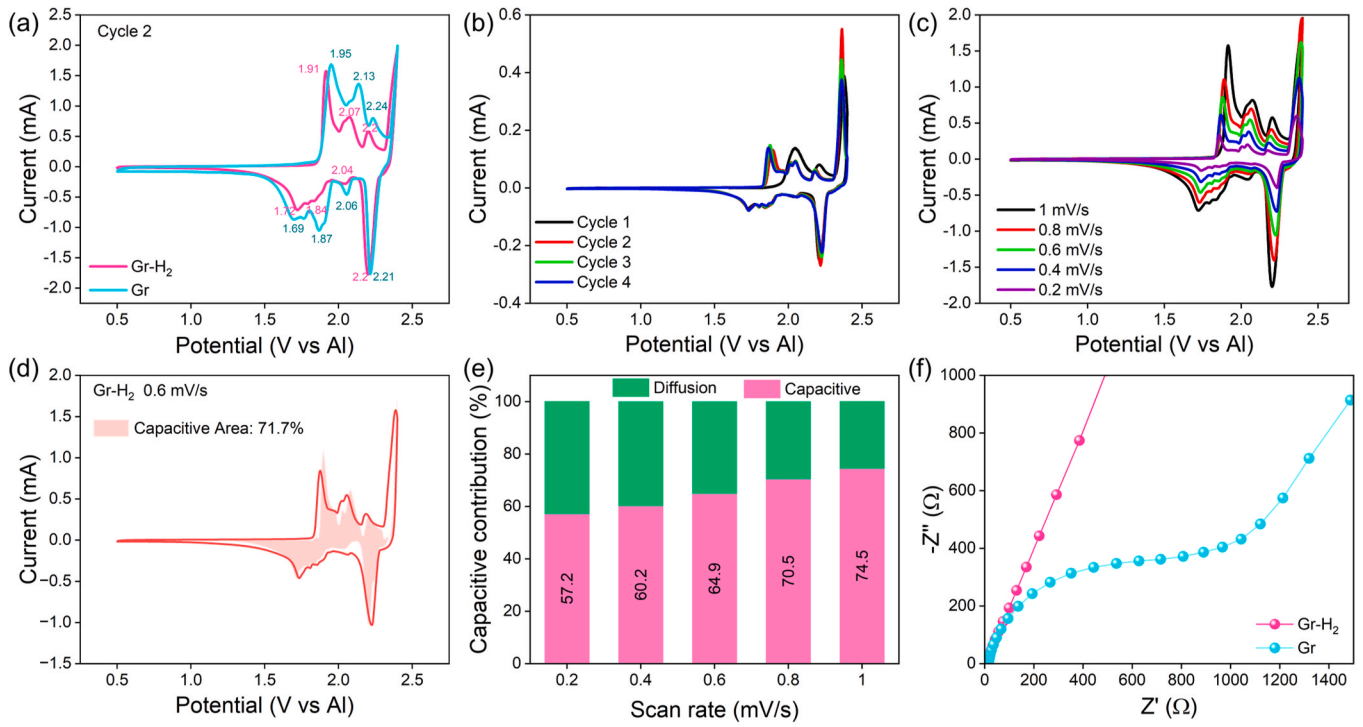

Fig. 5. Understanding the electrochemical charge storage mechanism in the graphite AIB (a) CV curves of Gr and Gr-H_2; (b) the first four CV curves of Gr-H_2; (c) CV curves of Gr-H_2 samples under different scan rates; (d and e) the capacitive contribution of Gr-H_2, and corresponding contribution ratio; (f) EIS of Gr and Gr-H_2.

control and adsorption capacitance control can be expressed by formula 1:

$$i(v) = i_{cap} + i_{diff} = k_1 v + k_2 v^{1/2} \quad (1)$$

Where $i(v)$ is the current (mA), v is the different scan rates (mV/s), k_1 and k_2 are the constants [33,34]. Based on that, the calculation results are given in Fig. 5d and e. At a scan rate of 0.6 mV/s, the contribution of adsorption capacitance is 71.7 %. When increasing the scan rate from 0.2 to 0.4, 0.6, 0.8, and 1 mV/s, the contribution rates of adsorption capacitance are also increasing from 64.0 % to 67.2 %, 71.3 %, 77.3 %, and 82.9 % (Figure S9 and Fig. 5e). The higher adsorption capacitance contribution at a higher rate indicates the abundant active sites at the surface of hydrogen plasma-treated graphite for efficient $AlCl_4^-$ anions transport [35].

To gain insight into the charge transfer resistance of the materials during the electrochemical reaction, the EIS of the Gr and Gr-H_2 were recorded and illustrated in Fig. 5f and Fig. S10. Using equivalent circuit analysis to fit the actual measured impedance data, where R_s represents the resistance of the solution; R_{SEI} and CPE_{SEI} represent the SEI film resistance and capacitance formed on the electrode, respectively; R_{ct} and CPE_d represent the charge transfer resistance and double-layer capacitance, respectively, and W represents Warburg impedance. The R_s of Gr-H_2 and Gr are 12.13 Ω and 10.53 Ω, respectively. While the R_{SEI} for Gr-H_2 is 72.57 Ω, much lower than that of graphite, which is 344.3 Ω, indicating that the hydrogen plasma treatment helps to improve the stability of SEI layer formation. In addition, the R_{ct} is only 0.302 Ω for the Gr-H_2 cathode, significantly lower than Gr (272.1 Ω). Low charge resistance is beneficial for rapid $AlCl_4^-$ diffusion and charge transfer, which arises from the formation of abundant surface-active sites after plasma treatment [14].

The electrochemical performance of graphite after the plasma treatment demonstrates an enhanced charge storage performance with excellent stability. The surface analysis and structural characterisation indicate that the plasma treatment significantly improves the quality of graphite by the selective removal of a-C, which could enhance the intercalation process. Therefore, post-mortem surface analysis of the materials has been conducted to understand the intercalation process during the electrochemical reaction. The ex-situ Raman spectroscopy coupled with CV measurements at different stages for $AlCl_4^-$ anion intercalation/deintercalation into the Gr-H_2 cathode are carried out, as shown in Fig. 6a–b. For the charging process, 1.8 V, 2.0 V and 2.4 V correlated to the initial, partial and full $AlCl_4^-$ anion intercalation stages were selected. Simultaneously, 2.1 V and 1.6 V in the discharging process are chosen to represent the partial and full $AlCl_4^-$ deintercalation stages. When charged from pristine to 1.8 V (point 1) and 2.0 V (point 2), the G band of Gr-H_2 blue-shifted from 1579 cm^{-1} to 1584 cm^{-1}. As charged to 2.4 V (point 3), the peak further blue-shifted to 1610 cm^{-1}. As the cathode was discharged, the peaks gradually shifted back to 1586 cm^{-1} and 1584 cm^{-1} for 2.1 V (point 4) and 1.6 V (point 5), respectively. The results can be assigned to the intercalation/deintercalation compound into graphite, which is $AlCl_4^-$ anion in the charging process [35].

Ex-situ XPS was used to analyse the bonding configuration of Al and Cl species in the Gr-H_2 cathode during charging and discharging processes (Fig. 6c–d, Figure S11-13). The intercalation of chloroaluminate ions was confirmed by the appearance of Al and Cl peaks after charging [8,36]. Apparently, the Cl 2p peak was shifted from 199.0 eV to higher binding energy (199.6 eV) when charged to 2.0 V and 2.4 V. When discharged, the Cl peak shifted back to 199.4 eV at 2.1V and further to a lower binding energy (199.0 eV) at 1.6 V. Similarly, the Al 2p peak was shifted to higher binding energy (from 74.9 to 75.4 eV) during charging process and shifted back to lower binding energy (from 75.2 to 74.9 eV) when discharged. The change of the peaks can be explained by the intercalation and deintercalation of $AlCl_4^-$ anions. For the charging process, the chloroaluminate ions are inserted into the graphitic layers of the Gr-H_2 cathode, indicated by the higher binding energy of Al 2p and Cl 2p peaks. Reversely, the $AlCl_4^-$ anions are deintercalated from the Gr-H_2 cathode when discharged; therefore, the binding energy is lower for Al 2p and Cl 2p peaks.

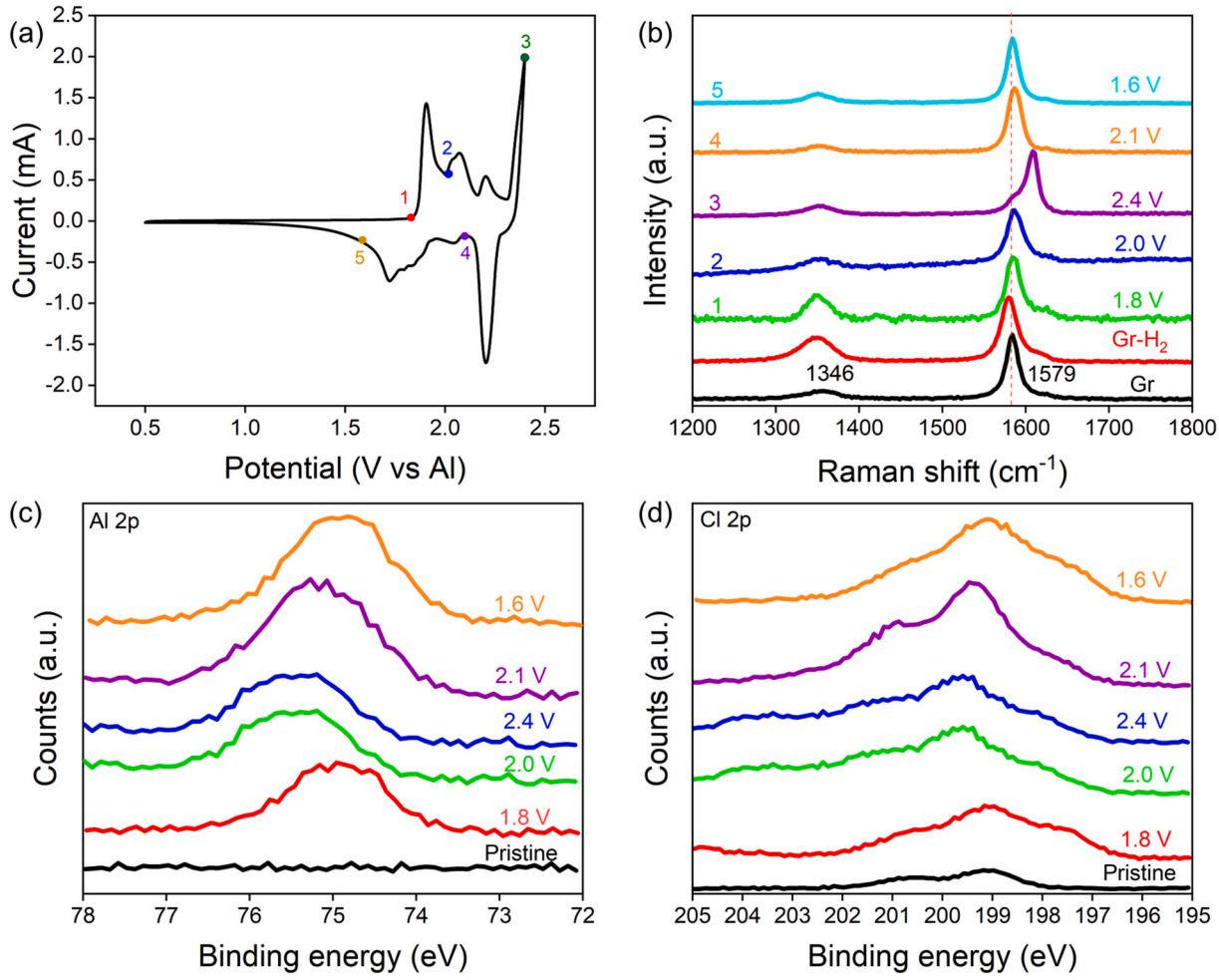

Fig. 6. Ex-situ characterisation on Gr-H_2 cathode: (a) CV curve of Gr-H_2 cathode for ex-situ characterisation; (b) Ex-situ Raman spectra of Gr-H_2 cathode at different voltages during charge-discharge process; Ex-situ XPS spectra of (c) Al 2p; (d) Cl 2p of Gr-H_2 cathode at different voltages during charge-discharge process.

3.3. Computational analysis

A hexagonal graphite supercell with a d spacing of around 9.12 Å [37] to accommodate the $AlCl_4^-$ anion, and the d spacing is 4.56 Å between two graphene layers, was considered for the calculations. The $AlCl_4^-$ anion with a negatively charged tetrahedral molecule (more stable than the square planar geometry) [38] was optimised in vacuum with a net charge of −1 to obtain its most stable geometry. Further, an amorphous carbon graphite structure was generated using a random distribution of carbon atoms within a 10 × 10 × 10 Å cell. All structures were optimised with a plane wave cut-off of 400 eV and a convergence threshold of 10-4 eV. To accurately describe the weak interlayer forces in graphite layers, the DFT-D3 [39] method of Grimme was incorporated. Gamma-centred Monkhorst-Pack [40] K points meshes 5 5 1 for graphite and 1 1 1 for $AlCl_4^-$ anion were used for the relaxation. In contrast, the isolated anion was treated at the Γ point to account for long-range Coulomb interactions in the charged system. The intercalation energy was calculated using the mathematical relation.

$$E_{int} = E_{graphite+AlCl4-} - E_{Graphite} - E_{AlCl4-}$$

Each term corresponds to the total energy of the system.

The relaxed structure of $AlCl_4^-$ anion interacting with both amorphous and crystalline graphite layers is displayed in Fig. 7. It can be seen that the crystalline graphite (Fig. 7a), a well-defined layered structure, the $AlCl_4^-$ anion is adsorbed stably in the interlayer region, with minimal distortion. The inclusion of van der Waals interaction effectively captures the weak interlayer binding with graphite layers. The intercalated tetrahedral $AlCl_4^-$ anions were distorted by the pressure of graphite layers similar to work done by Di-Yan Wang et al. [41].

In contrast, in the case of amorphous graphite (Fig. 7b), the $AlCl_4^-$ anion occupies a larger interstitial void, with more interaction due to the disordered system environment. In the present calculations, amorphous graphite, where structure order is low, shows more negative intercalation energy (−1.22 eV), indicating stronger binding with $AlCl4^-$ anion, because the carbon atoms are at defective edges (with sp^2/sp^3) hybridized mix, and disordered surface may offer large area which can interact more strongly with intercalating ions. However, too strong binding can reduce reversibility, which needs further evaluation, and make it harder for the $AlCl_4^-$ anion to deintercalated during discharge, reducing the life cycle. On the other hand, crystalline graphite (high layered structure), with moderately less negative intercalation energy (−0.98 eV), gives a balance between binding strength and reversibility that supports faster ion transport and high potential stability under life cycling. The reason for less binding energy is that the full accommodation of $AlCl_4^-$ anion may be restricted due to π-π interaction between layers.

The computational calculations on the $AlCl_4^-$ anion interaction towards graphite layers are well-aligned with the experimental findings. The non-treated graphite shows lower affinity towards the intercalation, possibly due to the irreversible intercalation induced by the amorphous layers on the surface. After the H_2 plasma treatment, the surface became cleaner and most of the irreversible amorphous carbon layers for the intercalation were removed. This stimulates the affinity of $AlCl_4^-$ anion toward the graphite surface for the reversible intercalation and increases the charge storage performance. Such studies, validating experimental

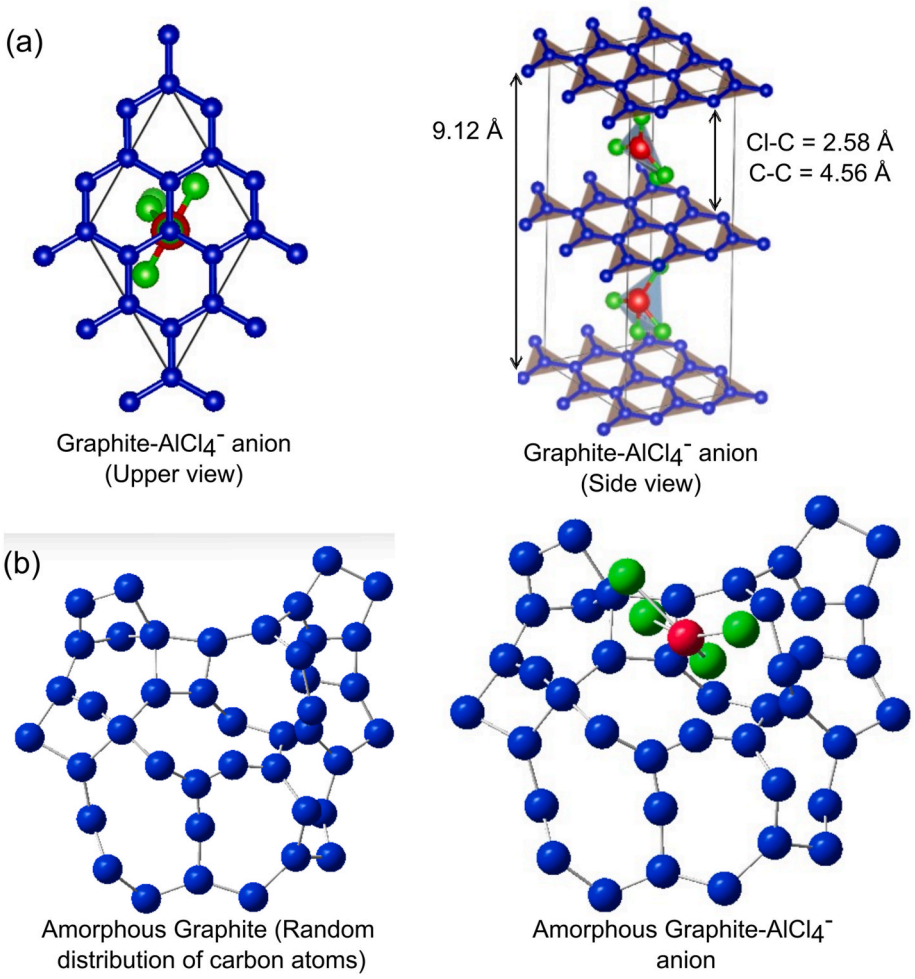

Fig. 7. Optimised geometries of graphite-$AlCl_4^-$ anion interaction (a) for the crystalline graphite; (b) amorphous carbon layer.

results by calculating the intercalation energies, would enable designing novel materials as a cathode for AIBs. We considered an interlayer spacing larger than the experimental value of 3.34 Å to account for the effect of $AlCl_4^-$ intercalation realistically. The ionic radius of $AlCl_4^-$ is about 5.28 Å, which is significantly larger than the graphite interlayer distance. During the first stage of intercalation, graphite layers undergo substantial expansion to accommodate these bulky anions. Therefore, using a larger interlayer spacing than the pristine graphite value provides a more accurate representation of the system under intercalation conditions, rather than the ideal pristine graphite structure.

4. Conclusion

In summary, we established a soft and dry plasma-assisted surface tailoring approach for enhancing the aluminium storage capabilities of graphite using hydrogen plasma. The electrochemical performance and storage mechanism of aluminium battery cells using plasma-treated graphite as cathode materials displayed enhanced intercalation and capacity. The galvanostatic charge-discharge tests reveal the outstanding performance for the hydrogen plasma-treated graphite with a high specific capacity (132.68 mAh/g at 50 mA/g) and remarkably high-rate performance (83.94 mAh/g at 1000 mA/g). We demonstrated that hydrogen plasma treatment can provide more accessible sites for $AlCl_4^-$, enhancing the specific capacity contributed by adsorption capacitance control in electrode materials. The ex-situ analysis further confirmed the strong interaction between chloroaluminate anions and the graphitic structure of Gr-H_2 when applied as the cathode for aluminium battery. Our results provide a useful perspective for developing surface modification of graphite for high-performance aluminium batteries and energy storage systems. Considering its simplicity and compatibility with existing battery manufacturing processes, the proposed plasma treatment strategy holds a promising route for integration into industrial electrode fabrication.

CRediT authorship contribution statement

Ruiqi Chen: Writing – original draft, Validation, Methodology, Formal analysis, Data curation. **Neelakandan M. Santhosh:** Writing – original draft, Methodology, Investigation, Formal analysis, Data curation, Conceptualization. **Janez Zavašnik:** Methodology, Investigation, Data curation. **Ravi Kumar Trivedi:** Methodology, Investigation, Formal analysis, Data curation, Computational simulation, analysis, and writing of the DFT part. **Saju Joseph:** Methodology, Investigation, Formal analysis, Data curation. **Komal Gola:** Methodology, Investigation, Data curation. **Nitish Kumar:** Methodology, Investigation, Formal analysis, Data curation. **Uroš Cvelbar:** Writing – original draft, Supervision, Resources, Funding acquisition. **Jinhua Sun:** Writing – review & editing, Writing – original draft, Supervision, Resources, Methodology, Investigation, Funding acquisition, Formal analysis, Conceptualization.

Declaration of competing interest

The authors declare the following financial interests/personal relationships which may be considered as potential competing interests:

Jinhua Sun reports financial support was provided by Chalmers University of Technology. Jinhua Sun reports a relationship with Chalmers University of Technology that includes: employment. If there are other authors, they declare that they have no known competing financial interests or personal relationships that could have appeared to influence the work reported in this paper.

Acknowledgements

This work was supported by the EU Graphene Flagship FLAG-ERA III JTC 2021 project "VEGA" (2021–05924, ANR-21-GRF1-0004 or MIZS-PR-11938), Chalmers Area of Advance-Production, 2D TECH VINNOVA competence Centre (2019-00068), JSI members thank the CENN center for the use of AFM Raman Imaging microscope for conducting the Raman analyses. NMS, JZ and UC acknowledge the financial support from the European Innovation Council Pathfinder project under ThermoDust grant agreement No. 101046835 and Slovenian Research Agency (ARIS) for the program No: P1-0417 and research grant J2-50074.

Appendix A. Supplementary data

Supplementary data to this article can be found online at https://doi.org/10.1016/j.carbon.2025.120835.

References

[1] T. Kim, W. Song, D.-Y. Son, L.K. Ono, Y. Qi, Lithium-ion batteries: outlook on present, future, and hybridized technologies, J. Mater. Chem. A 7 (7) (2019) 2942–2964.
[2] Y.X. Yao, X. Chen, N. Yao, J.H. Gao, G. Xu, J.F. Ding, C.L. Song, W.L. Cai, C. Yan, Q. Zhang, Unlocking charge transfer limitations for extreme fast charging of Li-ion batteries, Angew. Chem. Int. Ed. 62 (4) (2023) e202214828.
[3] H. Du, Y. Wang, Y. Kang, Y. Zhao, Y. Tian, X. Wang, Y. Tan, Z. Liang, J. Wozny, T. Li, D. Ren, L. Wang, X. He, P. Xiao, E. Mao, N. Tavajohi, F. Kang, B. Li, Side Reactions/Changes in lithium-ion batteries: mechanisms and strategies for creating safer and better batteries, Adv. Mater. 36 (29) (2024) 2401482.
[4] W. Fu, M. Aizudin, P.S. Lee, E.H. Ang, Recent progress in the applications of MXene-Based materials in multivalent ion batteries, Small 20 (47) (2024) 2404093.
[5] A. Mahmood, Z. Bai, T. Wang, Y. Lei, S. Wang, B. Sun, H. Khan, K. Khan, K. Sun, G. Wang, Enabling high-performance multivalent metal-ion batteries: current advances and future prospects, Chem. Soc. Rev. 54 (2025) 2369–2435.
[6] X. Yuan, Z. Lin, Y. Duan, Z. Chen, L. Fu, Y. Chen, L. Liu, X. Yuan, Y. Wu, Research progress, challenges, and prospects of high energy density aqueous aluminum-ion batteries: a mini-review, Batteries Supercaps 7 (9) (2024) e202400263.
[7] E. Hu, B.-E. Jia, W. Nong, C. Zhang, B. Zhu, D. Wu, J. Liu, C. Wu, S. Xi, D. Xia, M. Zhang, M.-F. Ng, A. Sumboja, K. Hippalgaonkar, Q. Yan, Boosting aluminum adsorption and deposition on single-atom catalysts in aqueous aluminum-ion battery, Adv. Energy Mater. 14 (34) (2024) 2401598.
[8] S. Wang, S. Jiao, W.-L. Song, H.-S. Chen, J. Tu, D. Tian, H. Jiao, C. Fu, D.-N. Fang, A novel dual-graphite aluminum-ion battery, Energy Storage Mater. 12 (2018) 119–127.
[9] J. Kim, M.R. Raj, G. Lee, High-defect-density graphite for superior-performance aluminum-ion batteries with ultra-fast charging and stable long life, Nano-Micro Lett. 13 (1) (2021) 171.
[10] J.H. Xu, D.E. Turney, A.L. Jadhav, R.J. Messinger, Effects of graphite structure and ion transport on the electrochemical properties of rechargeable aluminum–graphite batteries, ACS Appl. Energy Mater. 2 (11) (2019) 7799–7810.
[11] H. Chen, H. Xu, S. Wang, T. Huang, J. Xi, S. Cai, F. Guo, Z. Xu, W. Gao, C. Gao, Ultrafast all-climate aluminum-graphene battery with quarter-million cycle life, Sci. Adv. 3 (12) (2017) eaao7233.
[12] L. Zhang, L. Chen, H. Luo, X. Zhou, Z. Liu, Large-sized few-layer graphene enables an ultrafast and long-life aluminum-ion battery, Adv. Energy Mater. 7 (15) (2017) 1700034.
[13] K.V. Kravchyk, S. Wang, L. Piveteau, M.V. Kovalenko, Efficient aluminum chloride–natural graphite battery, Chem. Mater. 29 (10) (2017) 4484–4492.
[14] Z. Wang, D. Zhang, X. Bao, R. Hong, Y. Xu, J. Xu, T. Hsieh, Space-confined intercalation expansion strategy for simple and rapid synthesis of kish-based expanded graphite for aluminum ion batteries, Carbon 223 (2024) 119016.
[15] N.M. Santhosh, G. Filipič, E. Tatarova, O. Baranov, H. Kondo, M. Sekine, M. Hori, K. Ostrikov, U. Cvelbar, Oriented carbon nanostructures by plasma processing: recent advances and future challenges, Micromachines 9 (11) (2018) 565.
[16] Y. Zhang, D. Zhang, L. Zhang, B. Yang, Z. Gan, The etching mechanisms of diamond, graphite, and amorphous carbon by hydrogen plasma: a reactive molecular dynamics study, Adv. Theory Simulat. 6 (11) (2023) 2300371.
[17] Y. Wu, P. Qiao, T. Chong, Z. Shen, Carbon nanowalls grown by microwave plasma enhanced chemical vapor deposition, Adv. Mater. 14 (1) (2002) 64–67.
[18] S. Lee, J.-W. Peng, C.-H. Liu, Probing plasma-induced defect formation and oxidation in carbon nanotubes by Raman dispersion spectroscopy, Carbon 47 (15) (2009) 3488–3497.
[19] H. Hu, T. Cai, P. Bai, J. Xu, S. Ge, H. Hu, M. Wu, Q. Xue, Z. Yan, X. Gao, W. Xing, Small graphite nanoflakes as an advanced cathode material for aluminum ion batteries, Chem. Commun. 56 (10) (2020) 1593–1596.
[20] G.A. Elia, N.A. Kyeremateng, K. Marquardt, R. Hahn, An Aluminum/Graphite battery with ultra-high rate capability, Batteries Supercaps 2 (1) (2019) 83–90.
[21] D.-Y. Wang, C.-Y. Wei, M.-C. Lin, C.-J. Pan, H.-L. Chou, H.-A. Chen, M. Gong, Y. Wu, C. Yuan, M. Angell, Y.-J. Hsieh, Y.-H. Chen, C.-Y. Wen, C.-W. Chen, B.-J. Hwang, C.-C. Chen, H. Dai, Advanced rechargeable aluminium ion battery with a high-quality natural graphite cathode, Nat. Commun. 8 (1) (2017) 14283.
[22] Z. Li, J. Li, X. Li, W. Zhang, Pseudocapacitance effect in Al-C batteries with expanded graphite positive electrode at different temperatures, J. Power Sources 467 (2020) 228323.
[23] X. Dong, H. Xu, H. Chen, L. Wang, J. Wang, W. Fang, C. Chen, M. Salman, Z. Xu, C. Gao, Commercial expanded graphite as high-performance cathode for low-cost aluminum-ion battery, Carbon 148 (2019) 134–140.
[24] H. Sun, W. Wang, Z. Yu, Y. Yuan, S. Wang, S. Jiao, A new aluminium-ion battery with high voltage, high safety and low cost, Chem. Commun. 51 (59) (2015) 11892–11895.
[25] M.-C. Lin, M. Gong, B. Lu, Y. Wu, D.-Y. Wang, M. Guan, M. Angell, C. Chen, J. Yang, B.-J. Hwang, H. Dai, An ultrafast rechargeable aluminium-ion battery, Nature 520 (7547) (2015) 324–328.
[26] X. Yu, B. Wang, D. Gong, Z. Xu, B. Lu, Graphene nanoribbons on highly porous 3D graphene for high-capacity and ultrastable Al-Ion batteries, Adv. Mater. 29 (4) (2017) 1604118.
[27] D. Zhang, Z. Wang, X. Bao, R. Hong, X. Zhang, J. Xu, A green and low-cost approach to recover graphite for high-performance aluminum ion battery cathode, Mater. Today Sustain. 28 (2024) 100957.
[28] M. Angell, C.-J. Pan, Y. Rong, C. Yuan, M.-C. Lin, B.-J. Hwang, H. Dai, High coulombic efficiency aluminum-ion battery using an $AlCl_3$-urea ionic liquid analog electrolyte, Proc. Natl. Acad. Sci. 114 (5) (2017) 834–839.
[29] I. Weber, J. Schnaidt, B. Wang, T. Diemant, R.J. Behm, Model studies on the solid electrolyte interphase formation on graphite electrodes in ethylene carbonate and dimethyl carbonate: highly oriented pyrolytic graphite, Chemelectrochem 6 (19) (2019) 4985–4997.
[30] C. Yang, Y. Ma, X. Feng, H. Ning, S. Zhang, J. Li, C. An, Long-cycling and high-rate electrochemical performance of expanded graphite cathode materials with a two-stage aluminum storage mechanism, Sustain. Energy Fuels 5 (22) (2021) 5833–5842.
[31] Y. Yang, R. Zhao, Y.P. Chen, Expanded graphite with boron-doping for cathode materials of high-capacity and stable aluminum ion batteries, RSC Adv. 14 (33) (2024) 23902–23909.
[32] D. Chao, C. Zhu, P. Yang, X. Xia, J. Liu, J. Wang, X. Fan, S.V. Savilov, J. Lin, H. J. Fan, Z.X. Shen, Array of nanosheets render ultrafast and high-capacity Na-ion storage by tunable pseudocapacitance, Nat. Commun. 7 (1) (2016) 12122.
[33] P. Simon, Y. Gogotsi, B. Dunn, Where do batteries end and supercapacitors begin? Science 343 (6176) (2014) 1210–1211.
[34] T.C. Liu, W. Pell, B. Conway, S. Roberson, Behavior of molybdenum nitrides as materials for electrochemical capacitors: comparison with ruthenium oxide, J. Electrochem. Soc. 145 (6) (1998) 1882.
[35] S. Guo, H. Yang, M. Liu, X. Feng, Y. Gao, Y. Bai, C. Wu, Al-Storage behaviors of expanded graphite as high-rate and long-life cathode materials for rechargeable aluminum batteries, ACS Appl. Mater. Interfaces 13 (19) (2021) 22549–22558.
[36] W. Pan, Y. Wang, Y. Zhang, H.Y.H. Kwok, M. Wu, X. Zhao, D.Y. Leung, A low-cost and dendrite-free rechargeable aluminium-ion battery with superior performance, J. Mater. Chem. A 7 (29) (2019) 17420–17425.
[37] C.-J. Pan, C. Yuan, G. Zhu, Q. Zhang, C.-J. Huang, M.-C. Lin, M. Angell, B.-J. Hwang, P. Kaghazchi, H. Dai, An operando X-ray diffraction study of chloroaluminate anion-graphite intercalation in aluminum batteries, Proc. Natl. Acad. Sci. 115 (22) (2018) 5670–5675.
[38] P. Bhauriyal, A. Mahata, B. Pathak, The staging mechanism of AlCl 4 intercalation in a graphite electrode for an aluminium-ion battery, Phys. Chem. Chem. Phys. 19 (11) (2017) 7980–7989.
[39] S. Grimme, J. Antony, S. Ehrlich, H. Krieg, A consistent and accurate ab initio parametrization of density functional dispersion correction (DFT-D) for the 94 elements H-Pu, J. Chem. Phys. 132 (15) (2010).
[40] H.J. Monkhorst, J.D. Pack, Special points for Brillouin-zone integrations, Phys. Rev. B 13 (12) (1976) 5188.
[41] D.-Y. Wang, C.-Y. Wei, M.-C. Lin, C.-J. Pan, H.-L. Chou, H.-A. Chen, M. Gong, Y. Wu, C. Yuan, M. Angell, Advanced rechargeable aluminium ion battery with a high-quality natural graphite cathode, Nat. Commun. 8 (1) (2017) 14283.